ADVANCED ENERGY MATERIALS
www.advenergymat.de

3D Crystal Framework Regulation Enables Se-Functionalized Small Molecule Acceptors Achieve Over 19% Efficiency

Wei Gao, Ruijie Ma, Lei Zhu,* Lang Li, Francis R. Lin, Top Archie Dela Peña, Jiaying Wu, Mingjie Li, Wenkai Zhong, Xuefei Wu, Zachary Fink, Chengbo Tian, Feng Liu, Zhanhua Wei, Alex K.-Y. Jen,* and Gang Li**

Se-functionalized small molecule acceptors (SMAs) exhibit unique advantages in constructing materials with near-infrared absorption, but their photovoltaic performance lags behind that of S-containing analogs in organic solar cells (OSCs). Herein, two new Se-containing SMAs, namely Se-EH and Se-EHp, are designed and synthesized by regulating bifurcation site of outer alkyl chain, which enables Se-EH and Se-EHp to form different 3D crystal frameworks from CH1007. Se-EH displays tighter π–π stacking and denser packing framework with smaller-sized pore structure induced by larger steric hindrance effect of outer alkyl chain branched at 2-position, and a higher dielectric constant of PM6:Se-EH active layer can be obtained. OSCs based on PM6:Se-EH achieved very high PCEs of 18.58% in binary and 19.03% in ternary devices with a high FF approaching 80% for Se-containing SMAs. A more significant alkyl chain steric hindrance effect in Se-EH adjusts the molecular crystallization to form a favorable nanofiber interpenetrating network with an appropriate domain size to reduce rate of sub-ns recombination and promote balanced transport of carriers. This work provides references for further design and development of highly efficient Se-functionalized SMAs.

1. Introduction

Compared with inorganic silicon-based or organic-inorganic hybrid perovskite solar cells, organic solar cells (OSCs) have shown great advantages in being light, flexible, semitransparent, and stretchable, which makes OSCs technology very attractive for potential applications in future smart cities and building integrated photovoltaic (BIPV).[1–3] However, limited by the characteristics of organic semiconductors such as large exciton binding energy, short carrier lifetime, and low carrier mobility, OSCs often suffer from severe charge recombination and large energy loss (E_{loss}),[4,5] causing an unsatisfactory power conversion efficiencies (PCEs). What's exciting is that this dilemma has been broken with the discovery of two-star electron acceptor materials namely ITIC[6] and Y6,[7] which subsequently lead to a rapidly

W. Gao, L. Li, C. Tian, Z. Wei
Xiamen Key Laboratory of Optoelectronic Materials and Advanced Manufacturing
Institute of Luminescent Materials and Information Displays
College of Materials Science and Engineering
Huaqiao University
Xiamen 361021, China

R. Ma, G. Li
Department of Electrical and Electronic Engineering
Research Institute for Smart Energy (RISE)
The Hong Kong Polytechnic University
Hung Hom, Kowloon, Hong Kong 999077, China
E-mail: ruijie.ma@polyu.edu.hk; gang.w.li@polyu.edu.hk

L. Zhu, F. Liu
Frontiers Science Center for Transformative Molecules
In-situ Center for Physical Science
and Center of Hydrogen Science
School of Chemistry and Chemical Engineering
Shanghai Jiao Tong University
Shanghai 200240, China
E-mail: leizhu@sjtu.edu.cn

F. R. Lin, A. K.-Y. Jen
Department of Materials Science and Engineering
City University of Hong Kong
Kowloon, Hong Kong 999077, China
E-mail: alexjen@cityu.edu.hk

T. A. Dela Peña, M. Li
Department of Applied Physics
The Hong Kong Polytechnic University
Hung Hom, Kowloon, Hong Kong 999077, China

T. A. Dela Peña, J. Wu
Advanced Materials Thrust
Function Hub
The Hong Kong University of Science and Technology
Nansha, Guangzhou 511458, China

The ORCID identification number(s) for the author(s) of this article can be found under https://doi.org/10.1002/aenm.202304477

DOI: 10.1002/aenm.202304477

rising channel of PCEs of OSCs.[8] To date, single-junction and tandem OSCs devices have broken through 19%[9–29] and 20% PCE marks,[30–35] respectively, significantly narrowing the PCE gaps with other types of photovoltaic cells.

An active layer composed of a wide-bandgap donor that holds deep-lying highest occupied molecular orbital (HOMO) energy level and a near-infrared-absorbing narrow-bandgap electron acceptor is considered reasonable for pursuing high PCEs.[36] Acceptor–donor–acceptor (A–D–A) structured small molecule acceptors (SMAs) have made such type of architecture possible and work very well. As currently state-of-the-art electron acceptor materials, the success of Y6 and its derivatives is inseparable from smart molecular designs:[37] i) an electron-deficient benzo[*c*][1,2,5]thiadiazole (BT) unit is creatively incorporated into central π-core with effects of downshifting HOMO energy level for effective hole transfer and formation of a banana-shaped configuration for ordered 3D self-assembly with separated electron and hole transport channels respectively distributed in π-cores and end groups;[38] ii) two electron-rich pyrrole moieties are fused with BT to help broaden absorption range and potentially reduce E_{loss};[39] iii) the steric hindrance effect from two close alkyl chains anchored at *N* atoms of pyrrole leads to some molecular distortion to effectively inhibit excessive aggregation of SMDs; iv) outer alkyl chains flanking on thieno[3,2-*b*]thiophene not only improve molecular solubility but also can suppress configuration flip of vinyl.[40] Based on these understandings, fine-tuning of chemical structures at different sites of Y6 by employing reasonable design strategies has played critical roles in continuously promoting photovoltaic performance of Y6, which optimizes photon-absorbing, energy levels cascade and micro-nano morphology of active layers.[8]

Introducing functional heteroatoms, such as F, Cl, O, S, and Se atoms, into molecular backbone of organic semiconductors has been proven able to effectively adjust photoelectric and packing/aggregation properties of molecules.[41–45] Compared to S atom, Se atom shows stronger electron-donating ability due to a larger atomic radius and more abundant outer electrons, which makes it ideal for constructing near-infrared absorbing SMAs synchronously with stronger π–π stacking effects[46–52] due to enhanced quinoid character of multiple Se-substituted molecules for better molecular rigidity.[53] In previous works, a symmetric SMA CH1007 containing two Se atoms at either end of π-core was derived from Y6. The incorporation of Se atoms can not only reduce bandgap but also simultaneously enhance intermolecular π–π stacking, enabling OSCs to gain over 27 mA cm^{-2} short-circuit current (J_{SC}).[49] Subsequently, an asymmetric molecular design strategy was adopted to move a Se atom from central core to replace S atom on BT unit and constructed a pseudo-symmetric SMA BS3TSe-4F,[10] which properly lowers molecular crystallization property and also enhances the ability of free charge generation to significantly increase J_{SC} of a planar-mixed heterojunction OSC to over 29 mA cm^{-2}, demonstrating great potential of Se-functionalization in improving J_{SC} and PCE of OSCs. However, limited by synthesis difficulty, development of Se-containing SMAs lags far behind S-containing analogs that mainly manifested in their lower fill factor (FF) in devices.

Herein, two new SMAs namely Se-EH and Se-EHp were designed and synthesized by altering branched site of outer alkyl chain flanked on selenophene, attempting to fine-tune molecular packing and crystallinity so as to gain high FF and PCE in family of Se-functionalized SMAs. Outer alkyl chains changing from undecyl to 2-ethylhexyl (EH) or 3-ethylheptyl (EHp) will increase molecular bandgap but improve absorption coefficients with same orders of Se-EH > Se-EHp > CH1007. More importantly, such modification causes different single-crystal structures of SMAs, and the volume of unit cells gradually decreases from CH1007 to Se-EHp to Se-EH as the steric hindrance of outer alkyl chain becomes larger, tending to form denser molecular packing framework with shorter π–π stacking spacing and smaller-sized pore structure, which enables PM6:Se-EH and PM6:Se-EHp active layer a higher dielectric constant that is considered able to lower exciton binding energy (E_B^{CT}) of charge transfer (CT) state for more effective exciton dissociation.[54,55] Moreover, the steric hindrance effect of outer alkyl chain will cause stacking pattern of two molecules in one dimer to shift to a certain extent, thereby slowing down the crystallization rate of SMAs. Due to 2-position bifurcated alkyl chain owning largest steric hindrance, Se-EH exhibits slowest crystallization rate to form a favorable nanofiber interpenetrating network and a three-phase blend system with suitable domain size, which helps reduce the sub-ns recombination rate and promote balanced transport behavior. As a result, OSCs based on PM6:Se-EH achieved very high efficiencies of 18.58% in binary and 19.03% in ternary OSCs with a high FF approaching 80%. This work well illustrates the importance of steric hindrance effect from outer alkyl chain in regulating molecular packing/crystallinity to improve FF.

2. Results and Discussion

The synthetic routes and molecular structures of Se-EH and Se-EHp are displayed in **Scheme 1** with synthetic details and structural characterizations presented in Supporting Information (SI). These synthesis starts from a carboxylic acid with one more carbon atom than the targeted alkyl chains. An efficient Friedel-Crafts acylation reaction with tin tetrachloride as Lewis acid was performed between corresponding alkyl acid chlorides and ethyl 2-(thiophen-3-ylselanyl)acetate to offer two key intermediate compounds 1a and 1b. Subsequently, after undergoing three steps of intramolecular cyclization, decarboxylation, and tination reactions, two starting building blocks 3a and 3b were

W. Zhong
Institute of Polymer Optoelectronic Materials and Devices
State Key Laboratory of Luminescent Materials and Devices
South China University of Technology
Guangzhou 510640, China
X. Wu, Z. Fink
Materials Sciences Division
Lawrence Berkeley National Laboratory
Berkeley, CA 94720, USA
Z. Fink
Polymer Science and Engineering Department University of Massachusetts
Amherst, MA 01003, USA
A. K.-Y. Jen
Hong Kong Institute for Clean Energy
City University of Hong Kong
Kowloon, Hong Kong 999077, China

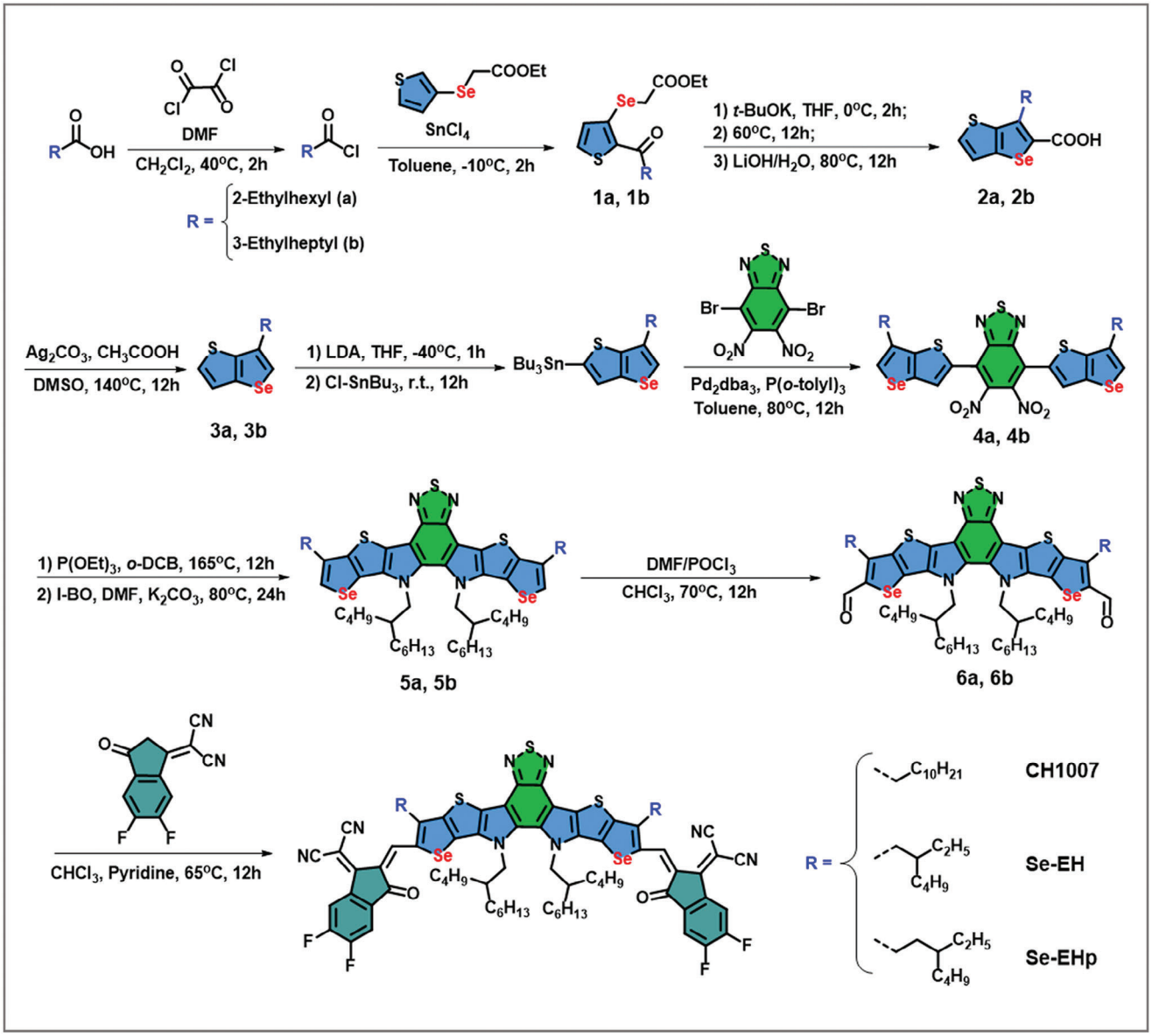

Scheme 1. Synthetic routes and molecular structures of CH1007, Se-EH, and Se-EHp.

obtained. The remaining synthetic steps are similar to those for the preparation of Y6. Additionally, CH1007 was also prepared for use as a control. All three SMAs show good solubility in commonly used processing solvents such as chloroform (CF). Thermogravimetric analysis (TGA) testing indicates good thermal stability of Se-EH, Se-EHp, and CH1007 with decomposition temperatures (T_d) of 5% mass being 338, 334, and 327 °C, respectively (Figure S1, Supporting Information).

UV-vis absorption spectra of CH1007, Se-EH, and Se-EHp dilute solution, neat and blend films were measured and shown in **Figures** 1a,b and S2 (Supporting Information), respectively, with extracted data summarized in **Table** 1. Since outer alkyl chain doesn't participate in the conjugation of molecular backbone, their absorption edges (λ_{onset}) in CF solution are basically the same with maximum absorption peaks (λ_{max}) located at 752 nm (Figure S2a, Supporting Information). However, alkyl chain altering from straight to bifurcated one obviously enhances the molar extinction coefficient (ϵ_{max}) of SMAs with an order of Se-EH (2.74×10^5 м$^{-1}$ cm^{-1}) > Se-EHp (2.18×10^5 м$^{-1}$ cm^{-1}) > CH1007 (1.89×10^5 м$^{-1}$ cm^{-1}) (Figure 1a), which is beneficial to increase J_{SC} in device. From solution to film state, Se-EH, Se-EHp, and CH1007 all exhibit large red-shifts of 67, 78, and 92 nm, respectively, with significant *0–1* vibration shoulder peaks, suggesting a strong molecular aggregation (Figure 1b). The absorption onsets of Se-EH, Se-EHp, and CH1007 were found to be 922, 932, and 943 nm, corresponding to optical bandgaps (E_g^{opt}) of 1.34, 1.33, and 1.31 eV, respectively. When blending polymer donor PM6 with SMA, molecular packing between each other will not be too much destroyed explained by well-maintained *0-0* and *0-1* vibration transition peaks of PM6 and SMAs from neat

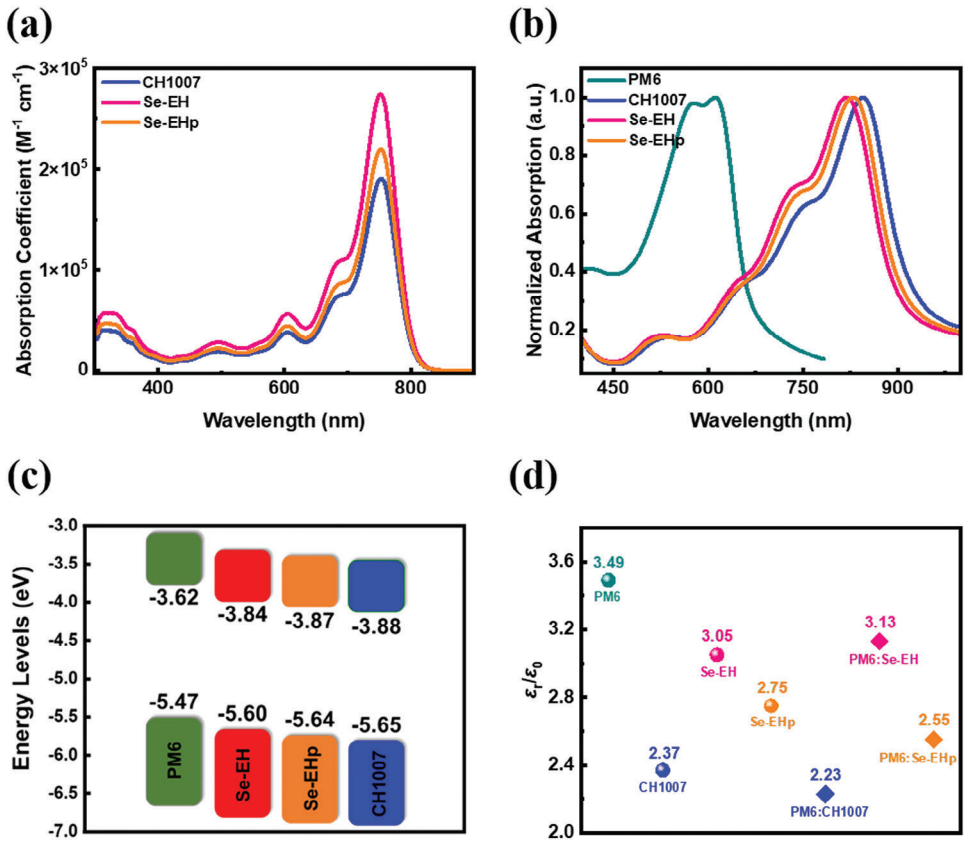

Figure 1. a) Molar extinction coefficient spectra of Se-EH, Se-EHp, and CH1007 in chloroform solution. b) Normalized UV–vis absorption spectra of PM6, Se-EH, Se-EHp, and CH1007 neat films. c) LUMO and HOMO energy levels of PM6, Se-EH, Se-EHp, and CH1007 films. d) Relative dielectric constants of PM6, Se-EH, Se-EHp, and CH1007 neat and blend films.

to blend films, which indicates a good morphological compatibility between PM6 and three SMAs (Figure S2b, Supporting Information).

Cyclic voltammetry (CV) measurements by using a three-electrodes system were employed to probe the lowest unoccupied molecular orbital (LUMO) and HOMO energy levels of Se-EH, Se-EHp, and CH1007 neat films spin-coated from CF solution (Figure S3, Supporting Information), which were calculated to be −3.84/−5.60, −3.87/−5.64, and −3.88/−5.65 eV, respectively (Figure 1c and Table 1). It shows that branched alkyl chain is able to elevate LUMO energy level of SMAs as compared to straight one, and 2-position branched alkyl chain behaves stronger LUMO-elevating effect than the branched alkyl chain at 3-position, which can be anticipated to gain higher open-circuit voltage (V_{OC}) in devices.[56]

In order to gain deep insights into the impacts of outer alkyl chain alteration on molecular packing, single crystals of Se-EH and Se-EHp were grown by using a three-solvent diffusion method as we reported previously for CH1007. Results of single-crystal structures of Se-EH and Se-EHp are shown in **Figure 2** with Oak Ridge thermal ellipsoid plot (ORTEP) provided in Figure S4 (Supporting Information) and corresponding crystallographic data listed in Tables S1 and S2 (Supporting Information), respectively. Se-EH adopts a triclinic system with a P −1 space group and contains two pairs of M/P enantiomers (M enantiomer shows counterclockwise from the high end to the low end, while P enantiomer shows clockwise from the high end to the low end) in a unit cell, which are similar to CH1007. The unit cell volume of Se-EH (7901 Å^3) is significantly smaller than that of CH1007 (9211 Å^3) due to decrease in lengths of b and c (a = 17.5, b = 18.

Table 1. Absorption and energy levels data for CH1007, Se-EH, and Se-EHp.

SMA	λ_{max} [a)] [nm]	λ_{onset} [a)] [nm]	ϵ_{max} [b)] [M^{-1} cm^{-1}]	λ_{max} [b)] [nm]	λ_{onset} [b)] [nm]	E_g^{opt} [c)] [eV]	LUMO [d)] [eV]	HOMO [d)] [eV]
Se-EH	752	807	2.74×10^5	819	922	1.345	−3.84	−5.60
Se-EHp	752	807	2.18×10^5	830	932	1.330	−3.87	−5.64
CH1007	752	807	1.89×10^5	844	943	1.315	−3.88	−5.65

[a)] In CF solution; [b)] Film spin-casted from CF solution; [c)] Calculated from empirical formula $E_g^{opt} = 1240/\lambda_{onset}$; [d)] Obtained from CV measurement.

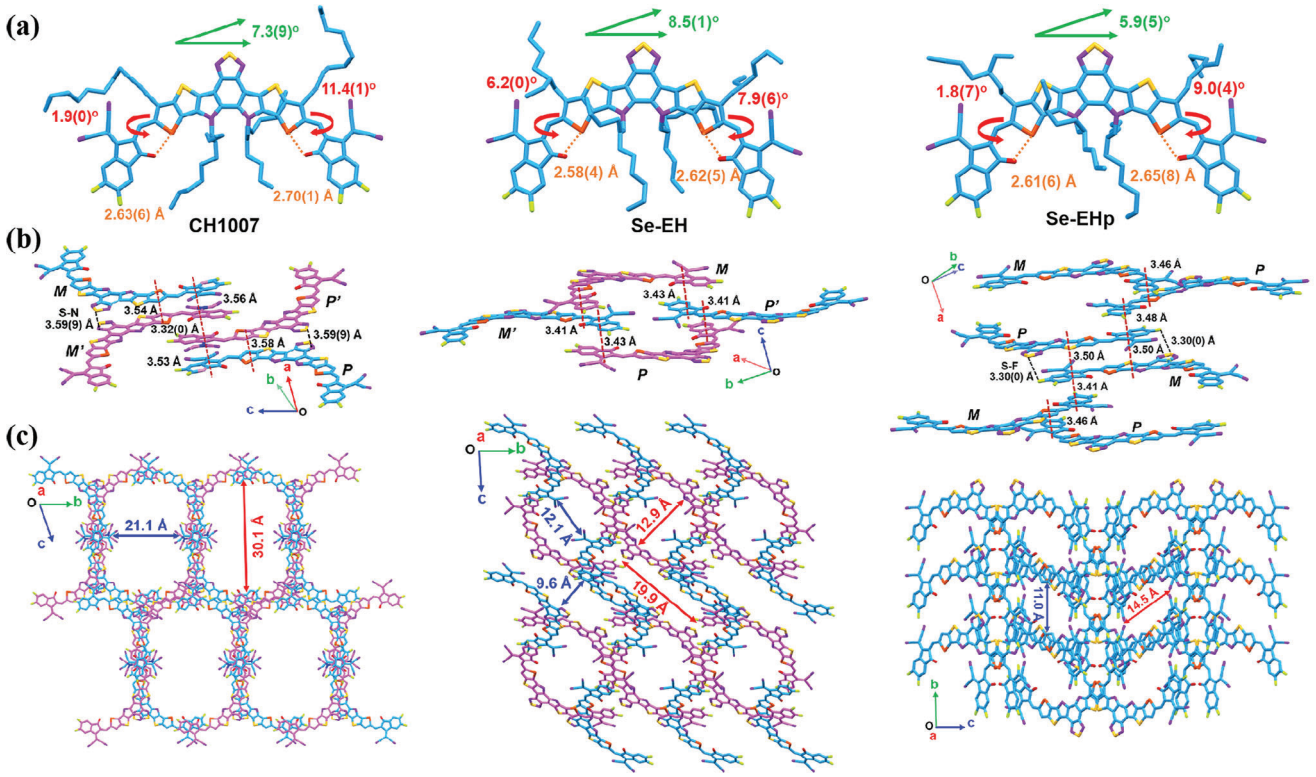

Figure 2. Single-crystal structures of CH1007, Se-EH, and Se-EHp: a) single molecules; b) π–π stacking pattern; c) 3D packing framework.

0, c = 27.8 Å for Se-EH and a = 13.6, b = 23.3, c = 31.3 Å for CH1007) and angles of β and γ ($\alpha = 85.3°$, $\beta = 77.0°$, $\gamma = 66.2°$ for Se-EH and $\alpha = 70.1°$, $\beta = 83.9°$, $\gamma = 80.7°$ for CH1007). While Se-EHp takes a monoclinic system with a C 2/c space group (a = 25.5, b = 20.8, c = 31.6 Å and $\alpha = 90°$, $\beta = 102.5°$, $\gamma = 90°$) and contains four groups of M/P enantiomer in a unit cell with a volume of 16 417 $Å^3$ which is less than twice the unit cell volume of CH1007 but larger than twice the unit cell volume of Se-EH. Moreover, crystal densities of CH1007, Se-EH, and Se-EHp were calculated to be 1.195, 1.337, and 1.296 g cm^{-3}, respectively.

Changes in outer alkyl chain of SMAs will cause slight perturbations in molecular configuration of individual molecules (Figure 2a). The D–A dihedral angles (measured from the two planes respectively built from the neighboring π-core selenophenyl and the five-membered ring of indanone on both sides of SMAs) of *M*/*P* enantiomers between end groups and π-core are found to be 1.9(0)°/11.4(1)° for CH1007, 6.2(0)° and 7.9(6)° for Se-EH and 1.8(7)°/9.0(4)° for Se-EHp with distances of intramolecular O-Se non-covalent interactions being 2.63(6)/2.70 (1) Å for CH1007, 2.58(4)/2.62 (5) Å for Se-EH and 2.61(6)/2.65 (8) Å for Se-EHp. Compared to CH1007, the torsion angles (measured from the two planes respectively built by the outward selenophenyl ring on different sides of the π-core) of π-core slightly increase in Se-EH from 7.3(9)° to 8.5(1)° but decrease in Se-EHp to 5.9(5)°. Moreover, molecular lengths measured from two farthest F atoms are 24.79(5), 23.22(2), and 24.29(0) Å for CH1007, Se-EH and Se-EHp, respectively. We speculate that above difference in single molecules of SMAs may be caused by a combined effect of alkyl chain bifurcation site (i.e., steric hindrance effect) and length. Most importantly, packing patterns of molecular single-crystals have been greatly affected by types of outer alkyl chains. CH1007 exhibits a similar stacking pattern to Y6 with four different dimers alternating between core-to-core and end-to-end stacking (Figure S5, Supporting Information). The end-to-end stacking distances of CH1007 between *M*/*M'*, *M'*/*P'* and *P'*/*P* are calculated to be ≈3.56, 3.32(0), and ≈3.53 Å, respectively (Figure 2b), and the core-to-core stacking distances between *M*/*M'* and *P'*/*P* are calculated to be ≈3.54 and ≈3.58 Å with an intermolecular S–N noncovalent interaction (distance of 3.59(9) Å), respectively (Figure 2b). While Se-EH shows three different dimers (Figure S6, Supporting Information) and presents two types of end-to-end stacking modes in unit cells with smaller distances of ≈3.43 Å for *M*/*P'* or *M'*/*P*, and ≈3.41 Å for *M*/*M'* or *P'*/*P* (Figure 2b). Se-EHp also owns three dimers similar to Se-EH (Figure S7, Supporting Information) but with only one pair of M/P enantiomer. Its stacking mode of unit cell is relatively complex and can be simply seen as a core-to-core stacking dimer inserted into Se-EH unit cell. The end-to-end or core-to-core stacking distances of Se-EHp are locked in 3.41–3.50 Å. In addition, an intermolecular S-F noncovalent interaction can be observed in core-to-core stacking mode of Se-EHp with a short distance of 3.30(0) Å. Due to differences in unit cell packing patterns, the 3D single-crystal frameworks of three SMAs are completely different, which are shown in Figure 2c and Figure S8 (Supporting Information) (different views of 3D packing frameworks of CH1007, Se-EH, and Se-EHp along a-, b-, and c-axis). Single-crystal framework of CH1007 shows a pore size of 20.1 × 30.1 Å, which is significantly larger than that of Se-EHp with a pore

size of 11.0 × 14.5 Å. While single-crystal framework of Se-EH shows two kinds of pores, an approximate square pore with a size of 12.1 × 12.9 Å and a rectangular pore with a size of 9.6 × 19.9 Å. It is worth mentioning that although the outer alkyl chains of Se-EH and L8-BO are similar and both 2-position branched (2-ethylhexyl for Se-EH and 2-butyloctyl for L8-BO), their 3D framework packing of single-crystals are completely different that L8-BO presents a round hole-like structure with a larger size of 16.8 × 20.8 Å.[57] Single-crystal analysis shows that outer alkyl chain transition from straight to branched one will change molecular single-crystal packing mode where bifurcated alkyl chain causes tighter molecular packing.

Differences in molecular packing often affect dielectric property of SMAs.[54] Dielectric constant as an important characteristic of photovoltaic materials determines exciton binding energy (E_B^{CT}) of charge transfer (CT) state according to Coulomb's law shown below:[54]

$$E_B^{CT} = \frac{q^2}{4\pi\varepsilon_0\varepsilon_r r} \quad (1)$$

where q is the elemental charge, ϵ_0 is the vacuum dielectric constant, ϵ_r is relative dielectric constant of surroundings and r is the average radius for electron-hole separation. To gain more insights into the influences of outer alkyl chain on dielectric constants of SMAs, capacitance (Cp) as a function of frequency was measured by using a capacitor architecture of indium tin oxide (ITO)/active layer/Ag with details regarding measurement displayed in Figure S9 and Table S3 (Supporting Information). ϵ_r values for CH1007, Se-EH, and Se-EHp were calculated to be 2.37, 3.05, and 2.75, respectively, under a frequency of 10^5 Hz where a flat capacitive response to frequency can be obtained, which is consistent with density of corresponding crystal. When polymer donor PM6 that has a ϵ_r of 3.49 was added in with a D:A weight of 1:1.2, the ϵ_r values of blend films based on PM6:CH1007 and PM6:Se-EHp became 2.23 and 2.55, respectively, lower than that for both components individually. While ϵ_r for PM6:Se-EH is 3.13, higher than that for pure Se-EH but slightly lower than that for PM6. As higher dielectric constant generally relates to more ordered molecular arrangement, the reason for this phenomenon is probably that PM6 addition causes less damage to ordered packing of Se-EH. Moreover, we also estimated the E_B^{CT} of neat and blend films based on retrieved ϵ_r and an approximate $r = 1.5$ nm[10] for CT state exciton according to formula (1), which are 0.275, 0.405, 0.314, and 0.349 eV for PM6, CH1007, Se-EH, and Se-EHp neat films, and 0.430, 0.307, and 0.376 eV for PM6:CH1007, PM6:Se-EH, and PM6:Se-EHp blend films, respectively. 2-Position branched alkyl chain shows a stronger ability in increasing ϵ_r than the 3-position branched one, which decreases E_B^{CT} of active layer thereby beneficial to improving exciton dissociation efficiency and reducing charge recombination for higher FF.[58]

It is known that the growth of single-crystal is a slow process and needs a long time, however, solid film can be quickly formed in a short time by spin-coating. Therefore, grazing incidence X-ray diffraction (GIXD) measurement was performed to probe difference of molecular packing/aggregation properties of three SMAs in neat films. 2D-GIXD patterns and corresponding cut-line profiles are shown in **Figure 3** with extracted parameters summarized in Table S4 (Supporting Information). It can be observed that all samples exhibit strong diffraction signals in q_z direction, indicating a well-defined "face-on" orientation relative to substrate for three SMAs (Figure 3a–c). The π–π stacking d-spacing and coherence length (CL) of CH1007, Se-EH, and Se-EHp neat films were calculated by fitting cut-line profiles using Lorentzian methods, which are found to be 3.655/16.7, 3.647/14.8, and 3.649/16.2 Å, respectively, as shown in Figure 3e,f. Se-EH pure film achieves the smallest π–π stacking spacing, Se-EHp performs second, and CH1007 has the largest π–π stacking spacing, which is consistent with the trend observed in single-crystals. However, CL of π–π stacking behaves completely opposite. To figure out why, we performed an analysis of the smallest packing unit (dimer) that could exist in pure film.

As given by single-crystal, CH1007 processes four different dimers, namely dimer 1, dimer 2, dimer 3, and dimer 4, that construct the 3D packing framework of CH1007. However, with alkyl chain transformation from straight chain to branched one, dimer 4 disappears in the 3D packing framework of Se-EH and Se-EHp, which may be due that a weaker packing intensity of dimer 4 compared to other three is more likely to be destroyed when steric hindrance effect on molecular packing increases. Three common dimer patterns (dimer 1, dimer 2, and dimer 3) for CH1007, Se-EH, and Se-EHp are presented in **Figure 4** for comparison. Se-EH can be approximately regarded as an ethyl group substituted into 2-position of outer alkyl chain of CH1007, while Se-EHp can be further obtained by moving this group to 3-position. Therefore, the order of steric hindrance exerted by outer alkyl chain on molecular packing is Se-EH > Se-EHp > CH1007 due to size of ethyl group much larger than that of hydrogen atom. Dimer 1 of CH1007 shows excellent half-molecular parallel stacking with two thiazole units overlapping (the distance between S atoms on two thiazole units is 4.47(4) Å) along with forming a strong S–N non-covalent interaction, and good end-to-end stacking concentrated on five-membered ring of two end groups. However, such form of π–π stacking in dimer 1 of Se-EH and Se-EHp is almost completely destroyed (the distances between S atoms on two thiazole units are 10.01(1) Å for Se-EH and 10.49(9) Å for Se-EHp) with stacking neither on π-core nor on end group because dimer 1 of Se-EH and Se-EHp needs to overcome huge steric hindrance effect brought by two branched alkyl chains to form a dimer 1 like CH1007. Dimer 2 of CH1007 exhibits good end-to-end antiparallel stacking, which is located between five-membered rings of two end groups and between benzene ring of one end group and vinyl group of another SMA (the distance between N atom on cyano group of one molecule and F atom on another molecule is 3.83(8) Å). Steric hindrance effect of branched alkyl chain has less influence on such packing pattern of dimer 2. Dimer 2′s stacking of Se-EH is concentrated between two end groups of SMAs with benzene ring of one end group stacked on five-membered ring of another end group, but this stacking position will be biased (the distance between N atom on cyano group of one molecule and F atom on another molecule is 6.46(9) Å) because 2-position branched alkyl chain of one SMA will prevent the end group of another SMA from extending in the direction of greater packing. But this stacking mode can be improved in dimer 2 of Se-EHp due to smaller steric hindrance effect of 3-position branched alkyl chain (the distance between N atom on cyano group of one molecule and F atom on another molecule is 5.63(1) Å). Dimer

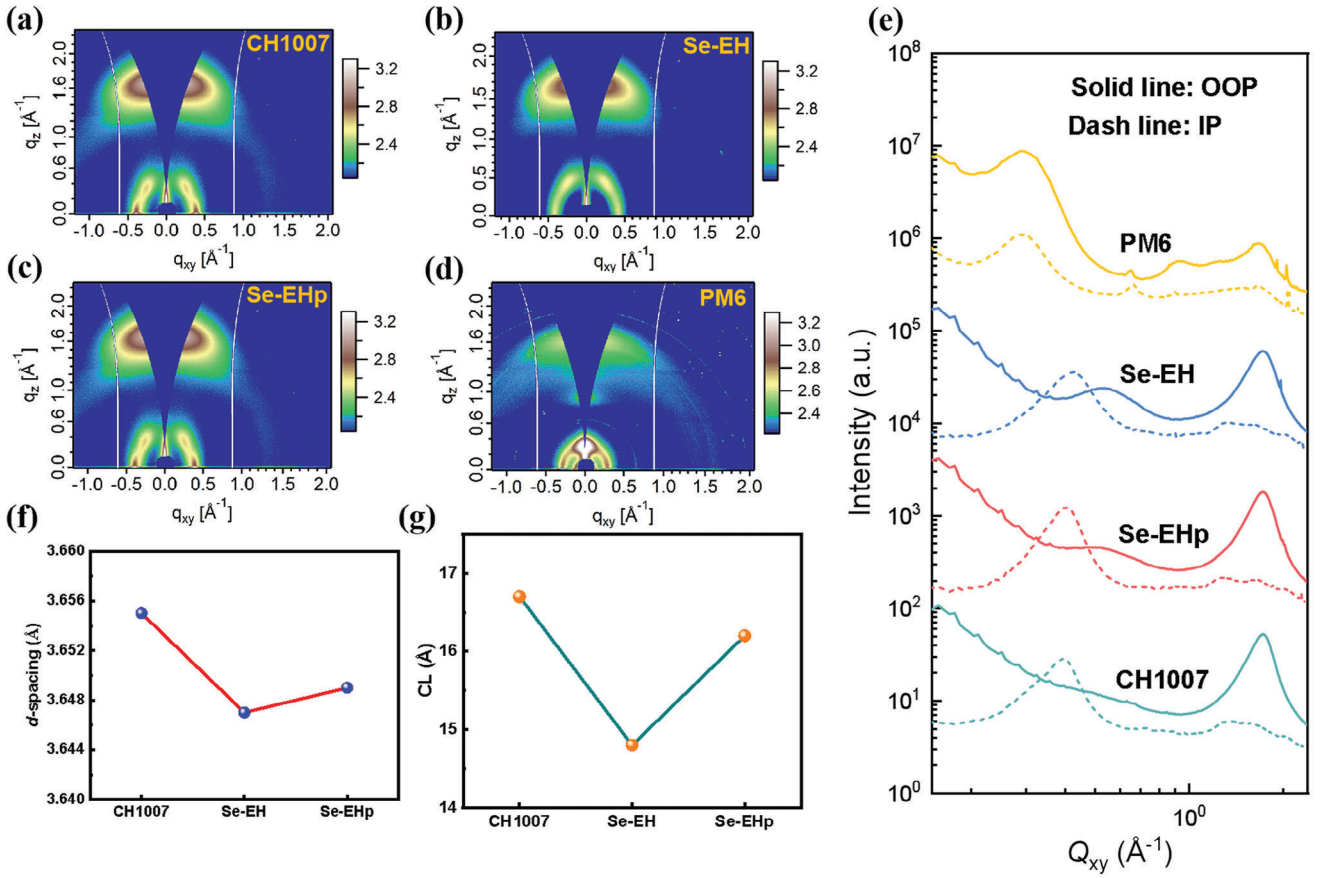

Figure 3. 2D GIXD patterns: a) CH1007; b) Se-EH; c) Se-EHp and d) PM6. e) Corresponding 1D line-cut profiles. f) *d*-spacing and g) CLs of CH1007, Se-EH, and Se-EHp neat films.

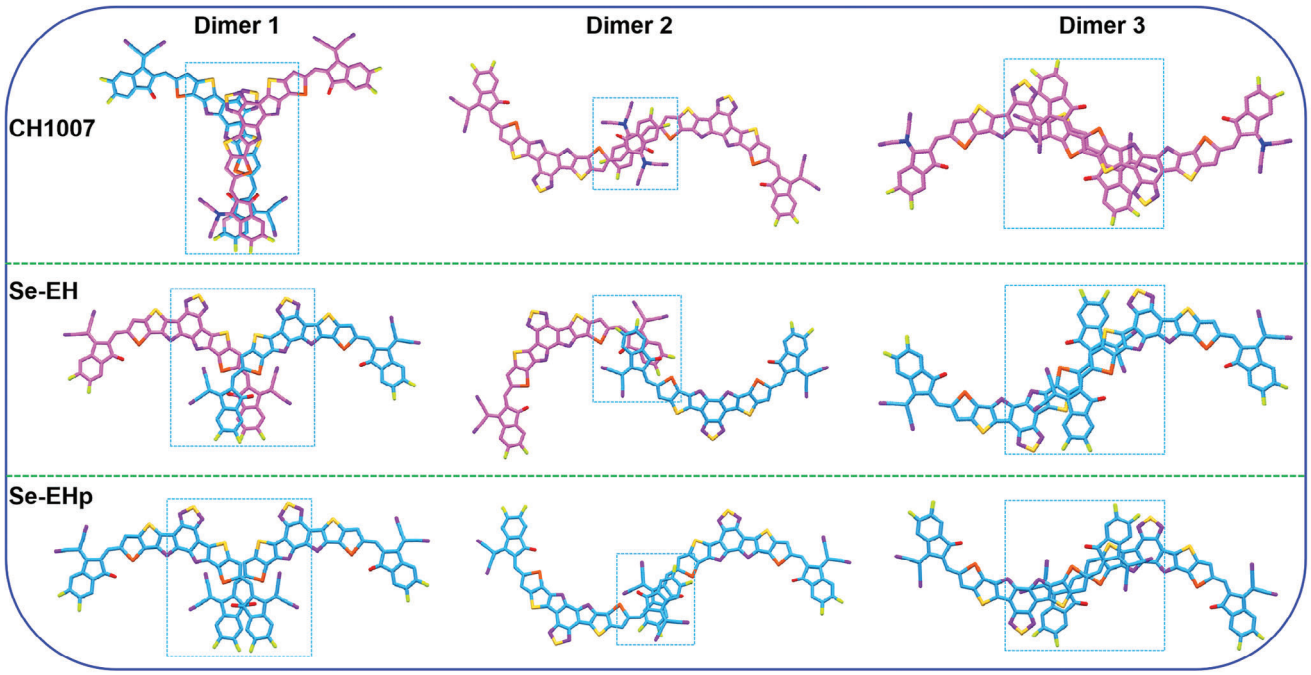

Figure 4. Different dimer patterns for CH1007, Se-EH, and Se-EHp.

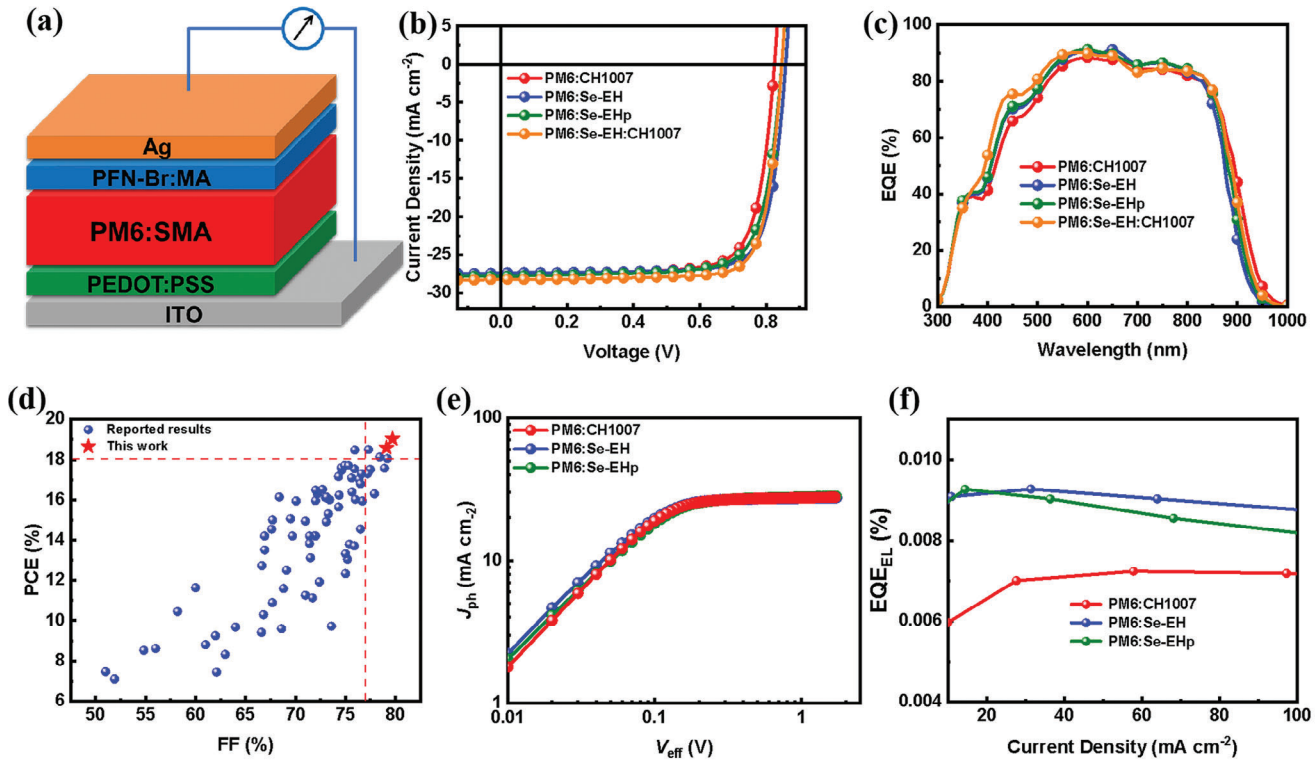

Figure 5. a) Device structure. b) Optimal *J*--*V* curves of OSCs based on PM6:CH1007, PM6:Se-EH, PM6:Se-EHp, and PM6:Se-EH:CH1007. c) Corresponding EQE spectra. d) FF and PCE statistics of Se-containing SMAs. e) J_{ph}–V_{eff} curves of PM6:CH1007-, PM6:Se-EH- and PM6:Se-EHp-based devices. f) EQE_{EL} plots.

3 of CH1007 exhibits an antiparallel stacking of half a molecule with benzene ring on end group of one SMA close to thiazole unit on π-core of another SMA (the distance between S atom on thiazole unit of one molecule and F atom on end group of another molecule is 3.29(1) Å). It can be observed that the benzene ring will become farther and farther away from thiazole unit as the steric hindrance of outer alkyl chain increases, especially in dimer 3 of Se-EH (the distances between S atom on thiazole unit of one molecule and F atom on end group of another molecule are 3.53(7) Å for Se-EH and 3.30(0) Å for Se-EHp). This steric hindrance effect of outer alkyl chain of SMA on molecular packing can also be clearly observed in differential scanning calorimeter (DSC) measurements (Figure S10, Supporting Information). Cold crystallization peaks with a crystallization temperature (*Tc*) of ≈206 °C appear in DSC curves of Se-EH and Se-EHp, while no such peak appears in the DSC curve of CH1007, which is likely because Se-EH and Se-EHp rearrange their internal structures by overcoming steric hindrance effect of outer alkyl chain from a disordered state to form an ordered crystal and release heat. This thermal-induced molecular rearrangement may make Se-EH and Se-EHp more ordered than CH1007, indicated by higher melting temperature of Se-EH (317 °C) and Se-EHp (313 °C) than that of CH1007 (303 °C). Moreover, the cold crystallization peak of Se-EH is significantly stronger than that of Se-EHp, indicating that the enthalpy change of Se-EH from a disordered state to a crystalline state is higher and Se-EH may become more ordered than Se-EHp after rearrangement, which is consistent with their melting temperature. The steric hindrance effect of alkyl chain flanked on selenophene of SMAs will reduce stacking effect of dimers, thereby decreasing CL of Se-EH and Se-EHp neat films in contrast to CH1007, which will to some extent reduce the crystalline features of SMAs (this can also be demonstrated by longer single-crystal growth cycles of Se-EH and Se-EHp). However, this steric effect in turn also helps large groups to be staggered from each other, such as cyano and carbonyl groups, conducive to achieving smaller molecular packing distances. More importantly, this steric hindrance effect changes configuration of dimers to form a denser 3D stacking framework with smaller-sized pore structures.

Photovoltaic performance of Se-EH and Se-EHp was investigated by fabricated OSCs devices with a conformation of ITO /poly(3,4-ethylenedioxythiophene):poly(styrenesulfonate)(PEDOT:PSS)/PM6:SMA/poly(9,9-bis(3-(*N*,*N*-dimethyl)-*N*-ethylammonium-propyl-2,7-fluorene)-*alt*-2,7-(9,9-dioctylfluorene))dibromide:Melamine (PFN-Br:MA)/Ag (**Figure** 5a). Specific procedures and conditions for device preparation can be found in Supporting Information. The optimal current density-voltage (*J*--*V*) curves of studied OSCs have been displayed in Figure 5b with photovoltaic parameters listed in **Table** 2. PM6:Se-EH-based OSCs are able to achieve a highest PCE of 18.58% coming from a V_{OC} of 0.859 V, a J_{SC} of 27.35 mA cm^{-2} and a FF of 79.1%. While OSCs enabled by PM6:Se-EHp gave secondary efficiency of 17.96% with a V_{OC} of 0.847 V, a J_{SC} of 27.79 mA cm^{-2} and a FF of 76.3%. However, both Se-EH and Se-EHp can obtain higher photovoltaic performance than CH1007 showing a PCE of 17.47% with a V_{OC} of 0.825 V, a J_{SC} of 27.50 mA cm^{-2} and

Table 2. Photovoltaic parameters of optimal OSCs based on PM6:CH1007, PM6:Se-EH, PM6:Se-EHp, and PM6:Se-EH:CH1007.

Active layer	V_{oc} [V]	J_{sc} [mA cm^{-2}]	J_{sc}[b)] [mA cm^{-2}]	FF [%]	PCE [%]
PM6:CH1007	0.825	27.50	26.62	77.0	17.47
PM6:Se-EH	0.859	27.35	26.55	79.1	18.58
PM6:Se-EHp	0.847	27.79	26.97	76.3	17.96
PM6:Se-EH:CH1007[a)]	0.847	28.19	27.30	79.7	19.03

[a)] Weight ratio of Se-EH:CH1007 is 0.8:0.4; [b)] Integrated J_{SC} from EQE spectra.

a FF of 77%. Outer alkyl chain regulation of SMAs can greatly enhance V_{OC} of devices by elevating LUMO energy levels of SMAs without causing too much loss to J_{SC} because Se-EH- and Se-EHp-based devices are able to achieve higher EQE response across entire test ranges although EQE spectra show blue-shifts (Figure 5c). The integrated J_{SC} from EQE spectra were measured to be 26.62, 26.55, and 26.97 mA cm^{-2} for CH1007-, Se-EH-, and Se-EHp-based devices, respectively, with small errors of ≈3%. In order to further improve PCE of Se-containing SMAs, we tried to add CH1007 as a third component into PM6:Se-EH to fabricate ternary OSCs, taking into account the possible complementary stacking between Se-EH and CH1007. Optimal weight ratio between Se-EH and CH1007 was screened from 1:0.2, 0.8:0.4 to 0.6:0.6 with *J*--*V* curves, EQE spectra, and photovoltaic parameters shown in Figure S11 and Table S5 (Supporting Information). As the proportion of CH1007 increases, the V_{OC}s of ternary devices slightly decrease with J_{SC}s first increasing and then reducing. Interestingly, FFs of ternary devices can be maintained at ≈79.6%. As a result, best-performing ternary OSCs based on PM6:Se-EH:CH1007 (1:0.8:0.4) were achieved with a PCE as high as 19.03% and a J_{SC} of 28.19 mA cm^{-2}. Compared with PM6:Se-EH binary devices, CH1007 addition is able to significantly improve EQE response within range of 350–550 nm, which is conducive to J_{SC} increase of ternary devices.

Se-functionalized SMAs have advantage of achieving high J_{SC}, but their FFs are generally difficult to exceed that of S-containing analogs. We have comprehensively counted reported OSCs based on Se-containing SMAs (Figure 5d; Table S6, Supporting Information) and found current dilemma for Se-based SMAs is that OSCs based on them are difficult to achieve more than 18% PCE and 77% FF. In this work, we significantly improved photovoltaic performance of Se-functionalized SAMs in both binary and ternary OSCs to 18.58% and 19.03% with high FF approaching 80%, which deserves one of the highest values reported so far.

Exciton dissociation and charge collection processes were explored by measuring photocurrent density (J_{ph}) against effective applied voltage (V_{eff})[59,60] (Figure 5e). J_{ph}–V_{eff} curves reveal that J_{ph} can quickly reach saturation (J_{sat}) at a small V_{eff} of 1.7 V, indicating a fast exciton dissociation process. And J_{sat}s are found to be 27.88, 27.62, and 28.27 mA cm^{-2} for PM6:CH1007-, PM6:Se-EH-, and PM6:Se-EHp-based devices, corresponding to exciton dissociation (P_{diss})/charge collection (P_{coll}) efficiencies of 98.6%/89.5%, 99.0%/90.9%, and 98.3%/88.3%, respectively, by calculating the specific values of J_{ph}/J_{sat} under short circuit and maximum power output conditions, respectively. More effective P_{diss} of PM6:Se-EH-based OSCs may be related to a smaller E_B^{CT} of PM6:Se-EH active layer and is conducive to achieving higher EQE. The higher P_{coll} is beneficial to improving FF of devices based on PM6:Se-EH. Moreover, *J*--*V* curves under different light intensities (P_{light}) were measured to determine recombination mechanism and degree of studied OSCs by analyzing J_{SC} and V_{OC} dependence on P_{light}.[59,60] It is observed that linear fitting of V_{oc}-ln(P_{light}) shows small slopes (α) close to kT/q (Figure S12a, Supporting Information), indicating that bimolecular recombination dominates in three devices. Furthermore, ln(J_{SC})–ln(P_{light}) fittings give similar slopes (S) with values approaching to 1.00 (Figure S12b, Supporting Information), demonstrating low degrees of bimolecular recombination happening in PM6:CH1007, PM6:Se-EH and PM6:Se-EHp devices, which is consistent with their high FF values.

Charge transport behaviors were also explored by employing electron-only (ITO/ZnO/active layer/PFN-Br:MA/Ag) and hole-only (ITO/PEDOT:PSS/active layer/MoO_3/Al) diodes[59,60] (Figure S13, Supporting Information). Electron (μ_e)/hole (μ_h) mobilities can be obtained by fitting *J*–*V* curves using space-charge-limited-current (SCLC) model based on ϵ_r obtained above. μ_es of neat CH1007, Se-EH, Se-EHp films and μ_h of PM6 film were calculated to be 1.17×10^{-2}, 5.17×10^{-3}, 7.44×10^{-3},and 3.88×10^{-3} cm^2 V^{-1} s^{-1}, respectively. Compared to CH1007, Se-EH, and Se-EHp exhibit relatively lower μ_e, which may be caused by larger dielectric constant and smaller CL that both originates from larger steric hindrance effect of outer branched alkyl chain, especially for Se-EH. When coming into blend films, μ_e, and μ_h all decrease relative to that of pure donor and acceptors due to a mutual destruction of molecular packing between donor and acceptor. μ_hs/μ_es of PM6:CH1007, PM6:Se-EH and PM6:Se-EHp active layers are 2.76×10^{-3}/5.41×10^{-4}, 5.42×10^{-4}/3.64×10^{-4} and 1.82×10^{-3}/4.94×10^{-4} cm^2 V^{-1} s^{-1} with μ_h/μ_e ratios of 5.10, 1.48, and 3.68, respectively. Significantly balanced electron/hole mobility of PM6:Se-EH contributes to its higher FF in devices.

To understand the effect of outer alkyl chain change on energy loss of OSCs, EQE onsets in long wavelength of optimal devices were fitted and bandgaps (E_gs) of PM6:Se-EH, PM6:Se-EHp, and PM6:CH1007 can be found to be 1.412, 1.383, and 1.367 eV, respectively. E_{loss} defined as difference between E_g and qV_{OC} ($E_{loss} = E_g - qV_{OC}$, where q is elementary charge) were estimated to be 0.553, 0.536, and 0.542 eV for PM6:Se-EH-, PM6:Se-EHp-, and PM6:CH1007-based devices, respectively, which suggests that Se-EH with 2-position branched outer alkyl chain will slightly increase E_{loss} of OSCs compared to CH1007, while the opposite is true for Se-EHp with 3-position branched outer alkyl chain. Moreover, the electroluminescence EQEs (EQE_{EL}) were also measured as shown in Figure 5f, which are 9.27×10^{-3} for PM6:Se-EH, 9.03×10^{-3} for PM6:Se-EHp and 7.24×10^{-3} for PM6:CH1007, corresponding to non-radiative E_{loss} ($\Delta E_3 = -kT \ln(EQE_{EL})$, where k is the Boltzmann constant and T is absolute temperature) of 0.241, 0.241, and 0.247 eV. This result reveals that optimization of outer alkyl chain by altering branched positions can inhibit non-radiation voltage loss to a certain extent and thus increase V_{OC} of relevant OSCs.

To gain further insights into the influences of outer alkyl chains on the morphology of active layer, atomic force

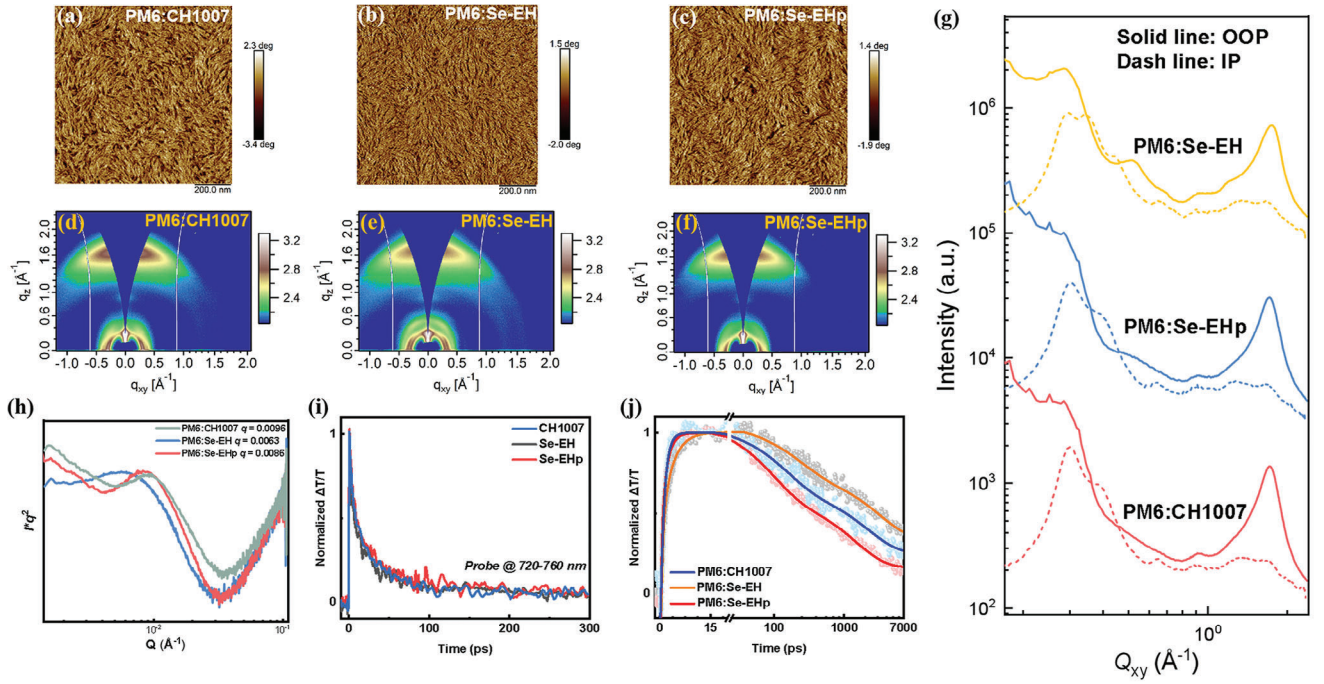

Figure 6. AFM phase images: a) PM6:CH1007; b) PM6:Se-EH; c) PM6:Se-EHp. 2D-GIXD patterns: d) PM6:CH1007; e) PM6:Se-EH; f) PM6:Se-EHp. g) Corresponding cut-line profiles. h) RSoXS measurements for PM6:CH1007, PM6:Se-EH, and PM6:Se-EHp blend films. TAS measurements for i) CH1007, Se-EH, and Se-EHp neat films and j) PM6:CH1007, PM6:Se-EH, and PM6:Se-EHp blend films.

microscope (AFM), contact angle (CA), transmission electron microscope (TEM), and GIXD measurements were performed with results shown in **Figure 6** and Figures S14–S17 (Supporting Information). AFM height images display a smooth and uniform surface for PM6:CH1007, PM6:Se-EH, and PM6:Se-EHp active layers with small root-mean-square (RMS) roughness of ≈1 nm (Figure S14, Supporting Information), which is conducive to good ohmic contact between active layer and metal electrode to obtain an efficient carrier extraction process. More importantly, it can be clearly observed from AFM phase images that PM6:Se-EH forms a denser (less voids) interpenetrating networks with finer nanofiber structure in contrast to PM6:CH1007 and PM6:Se-EHp, which can be attributed to a weaker crystallization property of Se-EH. Such type of morphology is considered to be beneficial to increase D-A interface and develop dual-continuous transport channels, which facilitates more effective exciton dissociation and balanced carrier transport to gain higher FF for PM6:Se-EH devices.

In addition, considering that outer alkyl chain altering may have an effect on surface tension of SMAs to change miscibility with polymer donor, contact angle measurements of neat films were performed (Figure S15, Supporting Information). Contact angles relative to surfaces of PM6, Se-EH, Se-EHp, and CH1007 neat films with water/ethylene glycol (EG) as media were found to be 106.1/81.3°, 97.7/66.2°, 99.1/66.8°, and 99.2/68.5°, respectively. According to Wu's model, surface energies of PM6, Se-EH, Se-EHp, and CH1007 were estimated to be 20.4, 28.2, 29.1, and 27.2 mN m^{-1}, respectively, which indicates that out alkyl chain from straight to bifurcated will slightly increase the surface energy of SMAs. Flory–Huggins interaction parameter χ that provides a direct information about the miscibility between two materials can be obtained by using Equation 2 suggested by Moons and co-workers[61]

$$\chi \propto (\sqrt{\gamma_A} - \sqrt{\gamma_B})^2 \quad (2)$$

where χ is Flory-Huggins interaction parameter between materials A and B, γ_A and γ_B are the surface energies of pure materials A and B, respectively. It shows that χ parameters of PM6:Se-EH, PM6:Se-EHp, and PM6:CH1007 differ slightly, which elucidates such change in out alkyl chain shows small impacts on the miscibility of SMAs with PM6. We further explored surface energies of PM6:Se-EH, PM6:Se-EHp, and PM6:CH1007 blend films considering that the surface energy of two components follows the following empirical formula (3):

$$\gamma_{AB} = X_1\gamma_A + X_2\gamma_B + X_1X_2\Delta\gamma \quad (3)$$

Where γ_{AB} is surface energy of two-component blend film of A and B, X_1 and X_2 are molar fractions of A and B, respectively, and $\Delta\gamma$ is the difference of surface energy between A and B. It is easy to calculate out the content of two components in the surface of blend film according to Equation 3 once the surface energy of blend films is measured. The water/EG contact angles were measured to be 105.9/75.4°, 105.0/76.7°, and 105.3/78.0° for PM6:Se-EH, PM6:Se-EHp and PM6:CH1007, respectively (Figure S16, Supporting Information), corresponding to surface energies of 27.6, 24.1, and 22.9 mN m^{-1} also fitting by using Wu's model. Therefore, contents of Se-EH, Se-EHp, and CH1007 in the surface of blend films of PM6:Se-EH, PM6:Se-EHp, and PM6:CH1007 were estimated to be 65%, 24%, and 21%, respectively, when assuming $X_1 + X_2 = 1$. It is obviously

higher that Se-EH content is almost three times than that of Se-EHp and CH1007 in the surface of blend films, which facilitates vertical phase separation of Se-EH component with high concentration at top electrode and is conducive to electron transport to cathode then to be effectively collected, thus helpful to FF improvement.

Subsequently, we performed TEM measurement to further confirm the aforementioned finding with images shown in Figure S17 (Supporting Information). It can be clearly observed that a significant increase in the proportion and domain size of the white region in TEM image of PM6:Se-EH compared to these of PM6:Se-EHp and PM6:CH1007, indicating crystalline phase component (e.g. SMA) is significantly enhanced in the surface of PM6:Se-EH blend film, which is highly consistent with the contact angle test results of blend films.

2D-GIXD patterns indicate that PM6:CH1007, PM6:Se-EH, and PM6:Se-EHp films all adopt favorable "face-on" orientations with strong (010) peaks in out-of-plane (OOP) direction and (100) peaks in in-plane direction (Figure 6d–f). The *d*-spacing/CL of π–π stacking are 3.64/20.8 Å for PM6:CH1007, 3.59/19.1 Å for PM6:Se-EH and 3.66/19.6 Å for PM6:CH1007. This smaller *d*-spacing and CL value of PM6:Se-EH film both should be caused by larger steric hindrance of outer alkyl chain of Se-EH. Smaller π–π stacking distance will promote intermolecular charge hopping for effective charge transfer between donor or acceptor molecules. CL value of PM6:Se-EH decrease causes hole and electron transport performance to simultaneously reduce but it does not affect balanced transport too much as revealed by SCLC results. The *d*-spacing/CL of lamellar packing for PM6, CH1007, Se-EH, and Se-EHp neat films in IP direction are fitted to be 21.4/37.7, 16.1/50.5, 14.9/38.5 and 15.7/52.9 Å, respectively. Se-EH owns smallest lamellar packing spacing that is consistent with its smallest unit cell volume. PM6 pure film exhibits a mixed orientation of "edge-on" and "face-on" (Figure 3d,e). Due to interaction with acceptor molecules, its molecular orientation changes into a complete "face-on" with π–π stacking signal (located at 1.676 $Å^{-1}$) overlapping with that of acceptor (located at 1.72 $Å^{-1}$) in blend film. Since there is a large difference in the lamellar packing distance between PM6 and SMAs, the donor and acceptor phases can be easily judged through this feature. PM6:CH1007 blend film exhibits two (100) diffraction peaks in the IP direction located at 0.300 and 0.385 $Å^{-1}$ (*d*-spacing of 20.9 and 16.3 Å), which can be attributed to the lamellar packing of PM6 and CH1007 phases, respectively. It can be seen that the lamellar packing of PM6 and CH1007 is less affected by each other, which is most likely because faster crystallization speed of CH1007 can squeeze PM6 all out of acceptor phase. For PM6:Se-EHp blend film, the lamellar packing of PM6 and Se-EHp phases in the IP direction also shows two (100) diffraction peaks located at 0.302 and 0.385 $Å^{-1}$ (*d*-spacing of 20.8 and 16.3 Å), respectively. However, the lamellar packing distance of Se-EHp in blend film is slightly larger than that in pure film, which can be attributed to a slightly slower crystallization rate of Se-EHp that cannot completely squeeze out PM6 when crystallizing and result in a small part of PM6 being mixed into acceptor phase to make lamellar packing spacing of Se-EHp become larger. PM6:Se-EH blend film displays three (100) diffraction peaks located at 0.291, 0.350, and 0.451 $Å^{-1}$ (*d*-spacing of 21.6, 18.0, and 13.9 Å), which can be classified as PM6 pure phase, PM6:Se-EH mixed phase and Se-EH pure phase, respectively. The formation of PM6:Se-EH mixed phase is probably due to the slower crystallization speed of Se-EH, making Se-EH co-crystallize with PM6.

Furthermore, different steric hindrance effects of outer alkyl chain on domain size of active layer were investigated by using resonant soft X-ray scattering (RSoXS) measurement (Figure 6h). RSoXS data revealed that scattering peaks of PM6:CH1007, PM6:Se-EH, and PM6:Se-EHp blend films are located at q = 0.0096, 0.0063, and 0.0086 $Å^{-1}$, corresponding to domain sizes of 32.7, 49.8, and 36.5 nm, respectively. This result indicates that the greater the steric hindrance effect of outer alkyl chain, the more conducive to the formation of a larger domain size, which is probably due to the steric hindrance effect of outer alkyl chain inhibiting crystallization of acceptor molecule to obtain a slower phase formation process, promoting the growth of domain size by prolonging crystallization time.

Femtosecond-resolved transient absorption spectroscopy (fs-TAS) of CH1007, Se-EH, and Se-EHp neat and blend films were performed to study the effect of morphological differences caused by steric hindrance of outer alkyl chain on dynamics of photo-induced charge carriers (Figure S18, Supporting Information). The excitation wavelength was determined as 800 nm according to their absorption spectra and a suitable excitation fluence of 3 μJ cm^{-2} for neat films and 5 μJ cm^{-2} for blend films was selected. We choose the fs-TAS spectral line-cuts immediately after excitation (i.e., 0.5–1.0 ps) to represent the single exciton that can be characterized by the ground state bleach (GSB) signal. The maximum GSB for SMAs is found to be located at 720–760 nm, thereby used as probe ranges. As shown in Figure 6i, there are no significant differences in the singlet exciton lifetime of CH1007, Se-EH, and Se-EHp as per 720–760 nm GSB kinetics indicates. But the GSB intensity of CH1007 appears weaker. It is not because of pump power fluctuation but apparently due to the weaker absorption (oscillator strength) of CH1007 as molar extinction coefficient indicates, thus leading to relatively smaller J_{SC} despite a narrower bandgap. The kinetics are based on the probe region, and its rise describes the exciton dissociation while the decay is for the sub-ns free charge recombination based on hole polarons photobleaching (PB). It can be observed in Figure 6j that PM6:Se-EH has the slowest exciton dissociation kinetics while PM6:Se-EHp and PM6:CH1007 blends are faster and comparable to each other, which is probably related to the mixed phase of PM6:Se-EH. Slower dissociation is not always harmful, as long the domain size is properly tuned, it can even be an advantage.[62] The rate of sub-ns recombination is PM6:Se-EHp > PM6:CH1007 > PM6:Se-EH. The faster recombination rate will compete with charge transport causing lower FFs, which very well correlates to the relative FFs obtained.

3. Conclusion

In summary, two new Se-functionalized SMAs Se-EH and Se-EHp respectively with 2-ethylhexyl and 3-ethylheptyl as outer alkyl chains were designed and synthesized. It was found that the steric hindrance of outer alkyl chain enables CH1007, Se-EH, and Se-EHp adopt completely different packing modes of unit cell and 3D crystal frameworks. The increase in steric hindrance of outer alkyl chain will cause stacking pattern of two molecules in one dimer to shift to a certain extent, which will stagger large

groups to reduce π–π stacking distance and also induce denser 3D molecular packing with smaller pore size and higher crystal density. Se-EH blend film achieved high dielectric constants to lower $E_B{}^{CT}$ and in turn improve exciton dissociation efficiency to help obtain high EQE response, allowing Se-EH to achieve higher V_{OC} without excessive loss of J_{SC} in devices. Moreover, the slower crystallization process of Se-EH promoted the formation of a suitable domain size with a favorable interpenetrating nanofiber network, which reduces the rate of sub-ns recombination and promotes balanced transport behavior, helping improve FF of Se-EH-based OSCs. As a result, PM6:Se-EH-based OSCs achieved 18.58% PCE in binary devices and 19.03% PCE in ternary devices, which both are one of highest values for Se-functionalized SMAs. Obvious photovoltaic performance improvement of Se-EH compared with classic Se-containing CH1007 revealed the importance of steric hindrance regulation of outer alkyl chains, and also illustrateed the feasibility of appropriately increasing steric hindrance effect to achieve high-performance SMAs by reducing molecular crystallinity.

Supporting Information

Supporting Information is available from the Wiley Online Library or from the author.

Acknowledgements

G.L. acknowledges the support from Research Grants Council of Hong Kong (Project Nos 15320216, 15221320, and C5037-18G), RGC Senior Research Fellowship Scheme (SRFS2223-5S01), National Natural Science Foundation of China (51961165102), Shenzhen Science and Technology Innovation Commission (JCYJ20200109105003940), the Hong Kong Polytechnic University Internal Research Funds: Sir Sze-yuen Chung Endowed Professorship Fund (8-8480), RISE (Q-CDA5), 1-W15V, 1-YW4C and Guangdong-Hong Kong-Macao Joint Laboratory for Photonic-Thermal-Electrical Energy Materials and Devices (GDSTC No. 2019B121205001). W.G. thanks for the support from Scientific Research Funds of Huaqiao University (605-50Y23024). R.M. thanks the PolyU Distinguished Postdoctoral Fellowship (1-YW4C).

Conflict of Interest

The authors declare no conflict of interest.

Author Contributions

W.G., R.M. A.K.-Y.J., and G.L. conceived the ideas. W.G. designed and synthesized the SMAs and carried out the UV–vis, CV, dielectric constant measurements, and single-crystal growth and resolution. L.L., C.T., and Z.W. assisted with part of the works of G.W. R.M. performed the device characterization and optimization, conducted the *J*–*V*, EQE, J_{ph}–V_{eff}, SCLC measurements, and fabricated the samples for morphology test. R.M., T.A.D.P., M.L., J.W., and G.L. performed the fs-TAS measurement and analyzed the data. L.Z., W.Z., X.W., Z.F., and F.L. conducted the AFM, GIXD and RSoXS measurements. W.G., R.M., F.R.L, Z.W., A.K.-Y.J., and G.L. contributed to the preparation of this manuscript. All authors have commented on this manuscript.

Data Availability Statement

The data that support the findings of this study are available from the corresponding author upon reasonable request.

Keywords

organic solar cells, selenium-functionalization, single-crystal, small molecule acceptor

Received: December 24, 2023
Revised: February 12, 2024
Published online: March 10, 2024

[1] H. Yu, J. Wang, Q. Zhou, J. Qin, Y. Wang, X. Lu, P. Cheng, *Chem. Soc. Rev.* **2023**, *52*, 4132.
[2] C. Yan, J. Qin, Y. Wang, G. Li, P. Cheng, *Adv. Energy Mater.* **2022**, *12*, 2201087.
[3] B. Liu, W. Xu, R. Ma, J.-W. Lee, T. A. D. Peña, W. Yang, B. Li, M. Li, J. Wu, Y. Wang, C. Zhang, J. Yang, J. Wang, S. Ning, Z. Wang, J. Li, H. Wang, G. Li, B. J. Kim, L. Niu, X. Guo, H. Sun, *Adv. Mater.* **2023**, *35*, 2308334.
[4] Y. Ji, L. Xu, X. Hao, K. Gao, *Sol. RRL* **2020**, *4*, 2000130.
[5] S. M. Menke, N. A. Ran, G. C. Bazan, R. H. Friend, *Joule* **2018**, *2*, 25.
[6] Y. Lin, J. Wang, Z.-G. Zhang, H. Bai, Y. Li, D. Zhu, X. Zhan, *Adv. Mater.* **2015**, *27*, 1170.
[7] J. Yuan, Y. Zhang, L. Zhou, G. Zhang, H.-L. Yip, T.-K. Lau, X. Lu, C. Zhu, H. Peng, P. A. Johnson, M. Leclerc, Y. Cao, J. Ulanski, Y. Li, Y. Zou, *Joule* **2019**, *3*, 1140.
[8] G. Zhang, F. R. Lin, F. Qi, T. Heumüller, A. Distler, H.-J. Egelhaaf, N. Li, P. C. Y. Chow, C. J. Brabec, A. K.-Y. Jen, H.-L. Yip, *Chem. Rev.* **2022**, *122*, 14180.
[9] Y. Wei, Z. Chen, G. Lu, N. Yu, C. Li, J. Gao, X. Gu, X. Hao, G. Lu, Z. Tang, J. Zhang, Z. Wei, X. Zhang, H. Huang, *Adv. Mater.* **2022**, *34*, 2204718.
[10] W. Gao, F. Qi, Z. Peng, F. R. Lin, K. Jiang, C. Zhong, W. Kaminsky, Z. Guan, C.-S. Lee, T. J. Marks, H. Ade, A. K.-Y. Jen, *Adv. Mater.* **2022**, *34*, 2202089.
[11] L. Zhu, M. Zhang, J. Xu, C. Li, J. Yan, G. Zhou, W. Zhong, T. Hao, J. Song, X. Xue, Z. Zhou, R. Zeng, H. Zhu, C.-C. Chen, R. C. I. MacKenzie, Y. Zou, J. Nelson, Y. Zhang, Y. Sun, F. Liu, *Nat. Mater.* **2022**, *21*, 656.
[12] Z. Chen, J. Zhu, D. Yang, W. Song, J. Shi, J. Ge, Y. Guo, X. Tong, F. Chen, Z. Ge, *Energy Environ. Sci.* **2023**, *16*, 3119.
[13] W. Zhang, Y. Wu, R. Ma, H. Fan, X. Li, H. Yang, C. Cui, Y. Li, *Angew. Chem., Int. Ed.* **2023**, *62*, 202309713.
[14] R. Ma, H. Li, T. A. D. Peña, X. Xie, P. W.-K. Fong, Q. Wei, C. Yan, J. Wu, P. Cheng, M. Li, G. Li, *Adv. Mater.* **2023**, *35*, 2304632.
[15] R. Ma, Q. Fan, T. A. D. Peña, B. Wu, H. Liu, Q. Wu, Q. Wei, J. Wu, X. Lu, M. Li, W. Ma, G. Li, *Adv. Mater.* **2023**, *35*, 2212275.
[16] T. Xu, Z. Luo, R. Ma, Z. Chen, T. A. D. Peña, H. Liu, Q. Wei, M. Li, C. Zhang, J. Wu, X. Lu, G. Li, C. Yang, *Angew. Chem., Int. Ed.* **2023**, *62*, e2023041; *Angew. Chem.* **2023**, *135*, 202304127.
[17] L. Kong, Z. Zhang, N. Zhao, Z. Cai, J. Zhang, M. Luo, X. Wang, M. Chen, W. Zhang, L. Zhang, Z. Wei, J. Chen, *Adv. Energy Mater.* **2023**, *13*, 2300763.
[18] S. Luo, C. Li, J. Zhang, X. Zou, H. Zhao, K. Ding, H. Huang, J. Song, J. Yi, H. Yu, K. S. Wong, G. Zhang, H. Ade, W. Ma, H. Hu, Y. Sun, H. Yan, *Nat. Commun.* **2023**, *14*, 6964.
[19] Z. Zhong, S. Chen, J. Zhao, J. Xie, K. Zhang, T. Jia, C. Zhu, J. Jing, Y. Liang, L. Hong, S. Zhu, D. Ma, F. Huang, *Adv. Energy Mater.* **2023**, *13*, 2302273.
[20] Z. Yao, X. Cao, X. Bi, T. He, Y. Li, X. Jia, H. Liang, Y. Guo, G. Long, B. Kan, C. Li, X. Wan, Y. Chen, *Angew. Chem., Int. Ed.* **2023**, *62*, 2023126.
[21] H. Lu, W. Liu, G. Ran, Z. Liang, H. Li, N. Wei, H. Wu, Z. Ma, Y. Liu, W. Zhang, X. Xu, Z. Bo, *Angew. Chem., Int. Ed.* **2023**, *62*, e2023144; *Angew. Chem.* **2023**, *135*, 2023144.

[22] B. Pang, C. Liao, X. Xu, L. Yu, R. Li, Q. Peng, *Adv. Mater.* **2023**, *35*, 2300631.
[23] C. Yang, M. Jiang, S. Wang, B. Zhang, P. Mao, H. Y. Woo, F. Zhang, J. Wang, Q. An, *Adv. Mater.* **2024**, *36*, 2305356.
[24] Z. Liu, M. Zhang, L. Zhang, S. Y. Jeong, S. Geng, H. Y. Woo, J. Zhang, F. Zhang, X. Ma, *Chem. Eng. J.* **2023**, *471*, 144711.
[25] Y. Zheng, T. Gao, S. Chen, C. T. J. Ferguson, K. A. I. Zhang, F. Fang, Y. Shen, N. A. Khan, L. Wang, L. Ye, *Compos. Commun.* **2022**, *36*, 101390.
[26] T. Chen, S. Li, Y. Li, Z. Chen, H. Wu, Y. Lin, Y. Gao, M. Wang, G. Ding, J. Min, Z. Ma, H. Zhu, L. Zuo, H. Chen, *Adv. Mater.* **2023**, *35*, 2300400.
[27] X. Yang, Y. Shao, S. Wang, M. Chen, B. Xiao, R. Sun, J. Min, *Adv. Mater.* **2023**, *35*, 2307863.
[28] R. Yu, R. Shi, Z. He, T. Zhang, S. Li, Q. Lv, S. Sha, C. Yang, J. Hou, Z. Tan, *Angew. Chem., Int. Ed.* **2023**, *62*, 2023083.
[29] K. Liu, Y. Jiang, F. Liu, G. Ran, F. Huang, W. Wang, W. Zhang, C. Zhang, J. Hou, X. Zhu, *Adv. Mater.* **2023**, *35*, 2300363.
[30] Z. Zheng, J. Wang, P. Bi, J. Ren, Y. Wang, Y. Yang, X. Liu, S. Zhang, J. Hou, *Joule* **2022**, *6*, 171.
[31] L. Meng, H. Liang, G. Song, M. Li, Y. Huang, C. Jiang, K. Zhang, F. Huang, Z. Yao, C. Li, X. Wan, Y. Chen, *Sci. China Chem.* **2023**, *66*, 808.
[32] G. Liu, R. Xia, Q. Huang, K. Zhang, Z. Hu, T. Jia, X. Liu, H.-L. Yip, F. Huang, *Adv. Funct. Mater.* **2021**, *31*, 2103283.
[33] J. Wang, Z. Zheng, P. Bi, Z. Chen, Y. Wang, X. Liu, S. Zhang, X. Hao, M. Zhang, Y. Li, J. Hou, *Natl. Sci. Rev.* **2023**, *10*, nwad085.
[34] L. Meng, Y. Zhang, X. Wan, C. Li, X. Zhang, Y. Wang, X. Ke, Z. Xiao, L. Ding, R. Xia, H.-L. Yip, Y. Cao, Y. Chen, *Science* **2018**, *361*, 1094.
[35] J. Wang, M. Zhang, J. Lin, Z. Zheng, L. Zhu, P. Bi, H. Liang, X. Guo, J. Wu, Y. Wang, L. Yu, J. Li, J. Lv, X. Liu, F. Liu, J. Hou, Y. Li, *Energy Environ. Sci.* **2022**, *15*, 1585.
[36] S. Chen, S. M. Lee, J. Xu, J. Lee, K. C. Lee, T. Hou, Y. Yang, M. Jeong, B. Lee, Y. Cho, S. Jung, J. Oh, Z.-G. Zhang, C. Zhang, M. Xiao, Y. Li, C. Yang, *Energy Environ. Sci.* **2018**, *11*, 2569.
[37] W. Gao, F. R. Lin, A. K.-Y. Jen, *Sol. RRL* **2022**, *6*, 2100868.
[38] G. Zhang, X.-K. Chen, J. Xiao, P. C. Y. Chow, M. Ren, G. Kupgan, X. Jiao, C. C. S. Chan, X. Du, R. Xia, Z. Chen, J. Yuan, Y. Zhang, S. Zhang, Y. Liu, Y. Zou, H. Yan, K. S. Wong, V. Coropceanu, N. Li, C. J. Brabec, J.-L. Bredas, H.-L. Yip, Y. Cao, *Nat. Commun.* **2020**, *11*, 3943.
[39] W. Gao, T. Liu, R. Sun, G. Zhang, Y. Xiao, R. Ma, C. Zhong, X. Lu, J. Min, H. Yan, C. Yang, *Adv. Sci.* **2020**, *7*, 1902657.
[40] Z. Zhang, J. Yu, X. Yin, Z. Hu, Y. Jiang, J. Sun, J. Zhou, F. Zhang, T. P. Russell, F. Liu, W. Tang, *Adv. Funct. Mater.* **2018**, *28*, 1705095.
[41] J.-S. Wu, S.-W. Cheng, Y.-J. Cheng, C.-S. Hsu, *Chem. Soc. Rev.* **2015**, *44*, 1113.
[42] Q. Zhao, J. Qu, F. He, *Adv. Sci.* **2020**, *7*, 2000509.
[43] H. Yao, L. Ye, H. Zhang, S. Li, S. Zhang, J. Hou, *Chem. Rev.* **2016**, *116*, 7397.
[44] B. Fan, F. Lin, X. Wu, Z. Zhu, A. K.-Y. Jen, *Acc. Chem. Res.* **2021**, *54*, 3906.
[45] H.-R. Bai, Q. An, M. Jiang, H. S. Ryu, J. Yang, X.-J. Zhou, H.-F. Zhi, C. Yang, X. Li, H. Y. Woo, J.-L. Wang, *Adv. Funct. Mater.* **2022**, *32*, 2200807.
[46] C. Yang, Q. An, M. Jiang, X. Ma, A. Mahmood, H. Zhang, X. Zhao, H.-F. Zhi, M. H. Jee, H. Y. Woo, X. Liao, D. Deng, Z. Wei, J.-L. Wang, *Angew. Chem., Int. Ed.* **2023**, *62*, 202313016.
[47] C. Yang, Q. An, H.-R. Bai, H.-F. Zhi, H. S. Ryu, A. Mahmood, X. Zhao, S. Zhang, H. Y. Woo, J.-L. Wang, *Angew. Chem., Int. Ed.* **2021**, *60*, 19241.
[48] J. Zhang, S. Luo, H. Zhao, X. Xu, X. Zou, A. Shang, J. Liang, F. Bai, Y. Chen, K. S. Wong, Z. Ma, W. Ma, H. Hu, Y. Chen, H. Yan, *Angew. Chem., Int. Ed.* **2022**, *61*, 202206930.
[49] F. Lin, K. Jiang, W. Kaminsky, Z. Zhu, A. K.-Y. Jen, *J. Am. Chem. Soc.* **2020**, *142*, 15246.
[50] Q. Fan, R. Ma, J. Yang, J. Gao, H. Bai, W. Su, Z. Liang, Y. Wu, L. Tang, Y. Li, Q. Wu, K. Wang, L. Yan, R. Zhang, F. Gao, G. Li, W. Ma, *Angew. Chem., Int. Ed.* **2023**, *62*, 202308307.
[51] Q. Fan, R. Ma, Z. Bi, X. Liao, B. Wu, S. Zhang, W. Su, J. Fang, C. Zhao, C. Yan, K. Chen, Y. Li, C. Gao, G. Li, W. Ma, *Adv. Funct. Mater.* **2023**, *33*, 2211385.
[52] X. Zhao, Q. An, H. Zhang, C. Yang, A. Mahmood, M. Jiang, M. H. Jee, B. Fu, S. Tian, H. Y. Woo, Y. Wang, J.-L. Wang, *Angew. Chem., Int. Ed.* **2023**, *62*, 202216340.
[53] S. S. Zade, N. Zamoshchik, M. Bendikov, *Chem. - Eur. J.* **2009**, *15*, 8613.
[54] T. M. Clarke, J. R. Durrant, *Chem. Rev.* **2010**, *110*, 6736.
[55] Z. Fu, X. Zhang, H. Zhang, Y. Li, H. Zhou, Y. Zhang, *Chin. J. Chem.* **2021**, *39*, 381.
[56] C. J. Brabec, A. Cravino, D. Meissner, N. S. Sariciftci, T. Fromherz, M. T. Rispens, L. Sanchez, J. C. Hummelen, *Adv. Funct. Mater.* **2001**, *11*, 374.
[57] C. Li, J. Zhou, J. Song, J. Xu, H. Zhang, X. Zhang, J. Guo, L. Zhu, D. Wei, G. Han, J. Min, Y. Zhang, Z. Xie, Y. Yi, H. Yan, F. Gao, F. Liu, Y. Sun, *Nat. Energy* **2021**, *6*, 614.
[58] X. Zhang, C. Li, J. Xu, R. Wang, J. Song, H. Zhang, Y. Li, Y.-N. Jing, S. Li, G. Wu, J. Zhou, X. Li, Y. Zhang, X. Li, J. Zhang, C. Zhang, H. Zhou, Y. Sun, Y. Zhang, *Joule* **2022**, *6*, 444.
[59] M. Jiang, H.-F. Zhi, B. Zhang, C. Yang, A. Mahmood, M. Zhang, H. Y. Woo, F. Zhang, J.-L. Wang, Q. An, *ACS Energy Lett.* **2023**, *8*, 1058.
[60] X. Song, Y. Song, H. Xu, S. Gao, Y. Wang, J. Li, J. Hai, W. Liu, W. Zhu, *Adv. Energy Mater.* **2023**, *13*, 2203009.
[61] S. Nilsson, A. Bernasik, A. Budkowski, E. Moons, *Macromolecules* **2007**, *40*, 8291.
[62] T. A. D. Peña, R. Ma, Z. Xing, Q. Wei, J. I. Khan, R. M. Young, Y. Hai, S. A. Garcia, X. Zou, Z. Jin, F. L. Ng, K. L. Yeung, D. F. Swearer, M. R. Wasielewski, J. Wang, H. Cha, H. Yan, K. S. Wong, G. Li, M. Li, J. Wu, *Energy Environ. Sci.* **2023**, *16*, 3416.